Chemical Engineering Journal 497 (2024) 154609

Contents lists available at ScienceDirect

Chemical Engineering Journal

journal homepage: www.elsevier.com/locate/cej

Dual-Salt aqueous electrolyte for enhancing Charge-Storage properties of VO_2 polymorphic cathodes for Zn-Ion batteries

Jing-Hong Huang [a,1], Xu-Feng Luo [b,1], Tzu-Yu Kuo [a,1], Yu-Hua Lai [a,1], Purna Chandra Rath [a], Chun-Wei Huang [a], Ming-Hsien Lin [c], An-Yuan Hou [a], Ju Li [d], Yu-Sheng Su [e], Wen-Wei Wu [a,*], Jeng-Kuei Chang [a,f,**]

[a] Department of Materials Science and Engineering, National Yang Ming Chiao Tung University, 1001 University Road, Hsinchu 30010, Taiwan
[b] National Synchrotron Radiation Research Center, 101 Hsin-Ann Road, Hsinchu 30076, Taiwan
[c] Department of Chemical and Materials Engineering, Chung Cheng Institute of Technology, National Defense University, Taiwan
[d] Department of Nuclear Science and Engineering and Department of Materials Science and Engineering, Massachusetts Institute of Technology, 77 Massachusetts Avenue, Cambridge, MA 02139, USA
[e] International College of Semiconductor Technology, National Yang Ming Chiao Tung University, 1001 University Road, Hsinchu 30010, Taiwan
[f] Department of Chemical Engineering, Chung Yuan Christian University, 200 Chung Pei Road, Taoyuan 32023, Taiwan

ARTICLE INFO

Keywords:
Electrolyte design
Polymorph
High concentration
Li salt
Wide-angle X-ray scattering
Operando transmission X-ray microscopy

ABSTRACT

Three VO_2 polymorphs, namely monoclinic VO_2 (B), monoclinic VO_2 (M), and tetragonal VO_2 (A), are synthesized, and their microstructures and electrochemical properties are studied for application in Zn-ion batteries (ZIBs). A cost-effective $ZnSO_4$-based aqueous electrolyte with various concentrations (3 − 7 m) of lithium bis (trifluoromethanesulfonyl)imide (LiTFSI) additive is developed. The optimal $ZnSO_4$/LiTFSI ratio in the electrolyte for superior Zn//VO_2 battery properties is examined. The coordination structures of various electrolytes are investigated using wide-angle X-ray scattering. The incorporation of LiTFSI impairs the hydrogen-bonded network of H_2O molecules and causes solvated-TFSI and TFSI···TFSI structures to form, altering the electrolyte properties (such as electrochemical stability window, ionic conductivity, and $Zn(OH)_2)_3(ZnSO_4)\cdot xH_2O$ byproduct formation tendency). It is found that an excessive LiTFSI concentration leads to the formation of ion aggregates in the electrolyte and thus deterioration of electrode specific capacity and rate capability. Operando transmission X-ray microscopy observations confirm the high dimensional stability of the VO_2 cathode during charging and discharging; the length variation of the VO_2 (B) rods is approximately 10 %. The electrolyte composition also affects the Zn^{2+}/Zn redox behavior at the anode side. The incorporation of LiTFSI into the electrolyte affects the Zn plating/stripping Coulombic efficiency, morphology of the deposited Zn, dead Zn amount, and anode cycle life. The constructed Zn//VO_2 (B) cell with 1 m $ZnSO_4$/5 m LiTFSI dual-salt electrolyte shows 90 % capacity retention after 1000 cycles. The proposed electrode material and electrolyte composition have great potential for applications in high-performance and high-stability rechargeable ZIBs.

1. Introduction

Fossil fuel shortages and emerging environmental issues have pushed the development of green energy technologies. However, the effective storage of intermittent renewable energy is still a challenge. Thus, it is imperative to explore advanced energy storage technologies that have high performance, good safety, and affordable cost [1–4]. Currently, Li-ion batteries occupy the majority of the commercial battery market; they are commonly used in portable electronic devices, electric vehicles, and large-scale energy storage systems [5,6]. However, lithium is scarce, and Li-ion batteries require a flammable organic electrolyte with low environmental benignity and face significant economic challenges and safety concerns for certain applications [7,8]. Among alternative rechargeable batteries, aqueous Zn-ion batteries (ZIBs) are promising owing to their

* Corresponding author.
** Corresponding author at: Department of Materials Science and Engineering, National Yang Ming Chiao Tung University, 1001 University Road, Hsinchu 30010, Taiwan.
E-mail addresses: wwwu@nycu.edu.tw (W.-W. Wu), jkchang@nycu.edu.tw (J.-K. Chang).
[1] Jing-Hong Huang, Xu-Feng Luo, Tzu-Yu Kuo, and Yu-Hua Lai contributed equally to this work.

https://doi.org/10.1016/j.cej.2024.154609
Received 21 February 2024; Received in revised form 28 July 2024; Accepted 5 August 2024
Available online 13 August 2024

low cost, high safety, and environmental friendliness. Zn is naturally abundant, and the Zn electrode has a low redox potential (–0.762 V vs. standard hydrogen electrode) and high theoretical capacity (820 mAh g^{-1}), making this electrode a promising candidate for large-scale energy storage applications [9–11]. Moreover, the aqueous electrolyte provides high ionic conductivity, which benefits the battery rate capability. Despite these advanced features, finding a good cathode material for ZIBs has been challenging. Manganese oxides, Prussian blue and its analogs, metal–organic frameworks, and organic compounds have been proposed as cathode materials for Zn ion storage [12–14]. Manganese oxide cathodes have a typical capacity of ~250 mAh g^{-1}, but manganese ions can easily dissolve in the electrolyte during cycling, leading to a short cycle life [15]. Prussian blue and its analogs are restricted by their low reversible capacities of 60–100 mAh g^{-1} [16]. Metal-organic framework materials tend to undergo pore collapse or pore size reduction during cycling, which could reduce their surface area and deteriorate their charge–discharge performance [17]. Organic cathodes could be soluble in the electrolyte, thereby contaminating the Zn metal anode and shortening cycle life [18]. Recently, vanadium-based cathodes, such as those made of vanadium phosphates, oxides, sulfides, nitrides, and vanadates, have attracted interest due to their open-framework crystal structures and the multiple oxidation states of vanadium [19–21]. Among the various compounds, vanadium dioxide (VO_2) is one of the most promising materials for ZIBs because it has a fast Zn^{2+} ion transport rate, high redox potential, high specific capacity, and easy synthesis [21–23].

Notably, VO_2 has a variety of crystal structures. With diverse precursors and synthesis routes, VO_2 can be fabricated in various polymorphs, including VO_2 (B), VO_2 (M), and VO_2 (A) [21]. VO_2 (B) belongs to the monoclinic structure of space group C2/m, in which an octahedra edge-sharing bilayer structure contains one-dimensional tunnels, allowing fast ion transport [21]. VO_2 (M) crystallizes into the monoclinic $P2_1/c$ space group with a tunnel structure via corner-sharing VO_6 octahedra. The structure contains alternating shorter (0.265 nm) and longer (0.312 nm) length V^{4+}–V^{4+} pairs along the *a* axis [19]. The VO_2 (A) phase has tetragonal symmetry and belongs to the $P4_2/ncm$ space group [24]. Zhang *et al.* synthesized various phases of VO_2 (B, M, and A) and compared their thermal behavior and oxidation resistance properties [25]. Srivastava *et al.* grew single-phase VO_2 (B), VO_2 (M), and VO_2 (A) films on $SrTiO_3$ substrates using a pulsed laser deposition technique and found that their electronic properties were clearly different [26]. The various VO_2 polymorphs have different channels and sites for Zn^{2+} diffusion and storage [21]; however, the charge–discharge properties of VO_2 (B), VO_2 (M), and VO_2 (A) have not been systematically compared, even though each phase has been individually examined. For example, Ding *et al.* demonstrated the hydrothermal synthesis of VO_2 (B) nanofibers and studied the pseudocapacitance behavior and ultrafast intercalation kinetics of Zn^{2+} ions in this structure. The reported capacity was ~350 mAh g^{-1} [27]. Zhang *et al.* integrated VO_2 (M) with carbon nanotubes to fabricate a binder-free self-standing ZIB cathode. This electrode delivered a capacity of 248 mAh g^{-1} at 2 A g^{-1}, with a corresponding Coulombic efficiency (CE) of 99.6 % [28]. Liu *et al.* synthesized polypyrrole-coated VO_2 (A) hollow nanospheres as a robust cathode material for ZIBs. The obtained material showed a high capacity of 440 mAh g^{-1} at 0.1 A g^{-1} [29]. However, it is difficult to compare the properties of VO_2 polymorphs based on papers with distinct experimental conditions. A systematic comparison of VO_2 (B), VO_2 (M), and VO_2 (A) is performed in the present study.

Electrolyte composition design plays a crucial role in enabling high-performance ZIBs. So far, various Zn-containing salts, including $ZnCl_2$, $Zn(NO_3)_2$, ZnF_2, $Zn(CH_3CO_2)_2$, $ZnSO_4$, $Zn(OTf)_2$ (OTf: CF_3SO_3), and Zn $(TFSI)_2$ (TFSI: $(CF_3SO_2)_2N$), have been investigated for application in ZIBs [30–32]. ZIBs with $Zn(OTf)_2$ and $Zn(TFSI)_2$ electrolytes have shown great performance in terms of rate capability and cyclability [31,32]. However, the high cost of $Zn(OTf)_2$ and $Zn(TFSI)_2$ is a great concern for practical applications. $ZnSO_4$ is another electrolyte solute frequently used for ZIBs because of its nontoxicity, high compatibility, and low cost [33,34]. Major drawbacks of the $ZnSO_4$ electrolyte are its narrow electrochemical stability window and significant side reactions [35,36]. The strong coordination between Zn^{2+} and solvated H_2O leads to the formation of bulky $[Zn(H_2O)_6]^{2+}$, which leads to slow ion transport [37]. The difficult desolvation of this complex ion can cause its co-insertion into the cathode host, leading to irreversible lattice expansion and eventual structural damage [37]. In addition, the large number of solvated H_2O molecules that are driven to the Zn electrode during charging could increase the hydrogen evolution reaction, Zn corrosion, and other side reactions [38]. To address these issues, additives such as $MnSO_4$, Li_2SO_4, and Na_2SO_4 have been coupled with $ZnSO_4$ to form a dual-salt electrolyte [39–41]. LiTFSI is selected for this study because of its high solubility and high chemical stability, which allow it to expand the electrochemical stability window of an aqueous electrolyte [42,43]. The use of a combination of $ZnSO_4$ and LiTFSI salts could be a promising strategy for boosting ZIB performance. However, to the best of our knowledge, the effects of LiTFSI addition into the $ZnSO_4$ electrolyte have not been previously investigated. This issue and the underlying mechanism are thus thoroughly examined herein.

In the present work, three VO_2 polymorphs, namely VO_2 (B), VO_2 (M), and VO_2 (A), are synthesized, and their microstructures and electrochemical properties are compared for possible application in ZIBs. LiTFSI at various concentrations (3 − 7 m; "m" is molality and is defined as the number of moles of solute per kilogram of the solvent) is incorporated into a cost-effective $ZnSO_4$-based electrolyte. The optimal $ZnSO_4$/LiTFSI ratio in the electrolyte for obtaining superior Zn//VO_2 battery performance is investigated. The electrolyte solvation chemistry is studied using wide-angle X-ray scattering (WAXS). The correlation between the solvation structure and the electrolyte properties (such as the generation of hydrogen and $Zn(OH)_2)_3(ZnSO_4)\cdot xH_2O$ byproducts) is explored. Operando transmission X-ray microscopy (TXM) is used to study the dimensional variation of the VO_2 cathode during charging/discharging. In addition to examinations on the cathode side, the influence of the electrolyte composition on the Zn anode performance (such as charge–discharge CE, cycling stability, and morphology change) is also analyzed.

2. Experimental procedures

2.1. Material synthesis

VO_2 samples were synthesized via the following reactions. 0.455 g of V_2O_5 was dispersed in 31 mL of deionized water, and then 2 mL of hydrogen peroxide and 2 mL of methanol were added into the solution, which was stirred for an hour at room temperature. The obtained brown $[VO(O_2)_2]^-$ solution was transferred into a 50-mL Teflon vessel to be heated in an oven at 180 °C for 48 h. This temperature has been found to be optimal for the synthesis of phase-pure VO_2 (B) [44]. The product was filtered and washed using deionized water and ethanol several times until a blue-black precipitate was obtained. After drying at 75 °C for 12 h, the VO_2 (B) sample was collected. VO_2 (A) was synthesized using a 40-mL aqueous dispersion with 0.6 g of the as-synthesized VO_2 (B), which was transferred into a Teflon vessel and then heated at 280 °C for 48 h. The black product denoted as VO_2 (A), was washed and dried using procedures similar to those described above. The synthesis of VO_2 (M) was carried out by heating the as-synthesized VO_2 (B) to 700 °C for 2 h at a heating rate of 5 °C min^{-1} in argon.

2.2. Material characterization

Microstructure and elemental analyses were conducted using scanning electron microscopy (SEM; JEOL JSM7800F Prime) and high-resolution transmission electron microscopy (TEM; JEOL F200). The TEM acceleration voltage was 200 kV. The energy-dispersive X-ray spectroscopy mapping was performed with a dwell time of 50 μs and a

resolution of 512 pixels × 512 pixels. Crystal structure characterization was carried out using X-ray diffraction (XRD; Bruker D2 Phaser) with Cu Kα radiation as the X-ray source.

2.3. Coin cell assembly

The cathode slurry was made by mixing the active material, Super P, and polyvinylidene fluoride binder in *N*-methylpyrrolidinone solution in a mass ratio of 7:2:1. The slurry was coated onto Ti foil with a doctor blade (200-μm gap height was used) and then dried in a vacuum oven at 80 °C for 8 h. The coated foil was then cut into circular electrodes with a diameter of 1.3 cm. The active material loading was approximately 2 mg cm^{-2}. $ZnSO_4$ salt with a concentration of either 1 or 3 m was used in the aqueous electrolyte. In addition, 3, 5, or 7 m LiTFSI was incorporated into the electrolyte to modify the electrolyte properties and the charge–discharge performance of the VO_2 electrodes. Coin cells with a CR2032 configuration were assembled with the prepared VO_2 electrodes, designed electrolytes, glass-fiber separators, and Zn metal sheets. The cell assembly was conducted under an ambient atmosphere.

2.4. Electrochemical evaluations

Linear sweep voltammetry (LSV) and cyclic voltammetry (CV) data were collected using a potentiostat (BioLogic BCS-810) at a potential scan rate of 1 mV s^{-1}. The charge–discharge properties, rate capability, and cycling stability of various Zn//VO_2 cells were assessed with a battery tester (Neware CT-4000) at 25 °C. All cells were cycled at 0.1 A g^{-1} three times in the formation process. Then, the specific capacity, CE values, and capacity retention at a certain rate or after cycling were evaluated. Electrochemical impedance spectroscopy (EIS) analysis was performed using a voltage perturbation amplitude of 10 mV within a frequency range of 10^6–10^{-2} Hz. The galvanostatic intermittent titration technique (GITT) was used to assess the ion diffusion coefficients (*D*) within various electrodes. A potentiostat (BioLogic VSP-300) was employed in the EIS and GITT measurements. To study the Zn plating/stripping behavior, Zn//Cu cells were used. Three conditioning cycles were applied before data collection. The deposition of Zn was conducted at 0.5 mA cm^{-2} for 1 h. Zn dissolution was then conducted at the same rate until a cutoff voltage of 1.0 V.

2.5. Synchrotron X-ray analyses

WAXS was performed at beamlines TPS25A1 and TLS23A1 at the National Synchrotron Radiation Research Center (NSRRC) in Taiwan. The WAXS patterns were acquired using 19-keV incident X-rays (wavelength = 0.65197 Å) and a sample-to-detector distance of 100.8 mm in transmission mode. Operando TXM was conducted at beamline TLS01B1 at NSRRC. High-flux X-rays with a photon energy of 5 keV passed through the coin cells with 2-mm holes covered with Kapton tape. The generated phase-contrast images were collected. Each TXM image (frame size: 15 μm × 15 μm) was acquired for at least 60 s to ensure high-quality data.

3. Results and discussion

The XRD pattern for the VO_2 (B) sample is shown in Fig. 1**a**. The strong crystalline peaks perfectly match those of monoclinic VO_2 (B) (JCPDS:65–7960). The XRD pattern for the VO_2 (M) sample is shown in Fig. 1**b**. It is consistent with JCPDS:72–0514. The XRD pattern for the VO_2 (A) sample is shown in Fig. 1**c**. It indicates that VO_2 (A) has a tetragonal structure that corresponds to JCPDS:42–0876. The crystallite sizes of VO_2 (B), VO_2 (M), and VO_2 (A) were calculated using the Scherrer equation [45] and were found to be 17 nm, 46 nm, and 37 nm, respectively. **Table S1** compares the crystal structures, space groups, and lattice parameters of the three VO_2 polymorphs. Fig. 1**d** shows the TEM analysis data for VO_2 (B). A nanowire morphology with a diameter of ~40 nm was observed. The energy-dispersive X-ray spectroscopy mapping results confirm that the V and O elements were homogeneously distributed in the sample. The *d* spacing of 0.37 nm found in the high-resolution lattice image is attributed to the (0 1 0) plane. The fast Fourier transform (FFT) pattern corresponds to the [0 0 1] zone axis of monoclinic VO_2 (B). As shown in Fig. 1**e**, the morphology of VO_2 (M) is spherical. The V and O signals are uniform across the oxide particles. The lattice image and FFT pattern verify the monoclinic crystal structure of VO_2 (M). The VO_2 (A) sample with a rod-like morphology was also examined with TEM; the data are shown in Fig. 1**f**. The rod diameter is

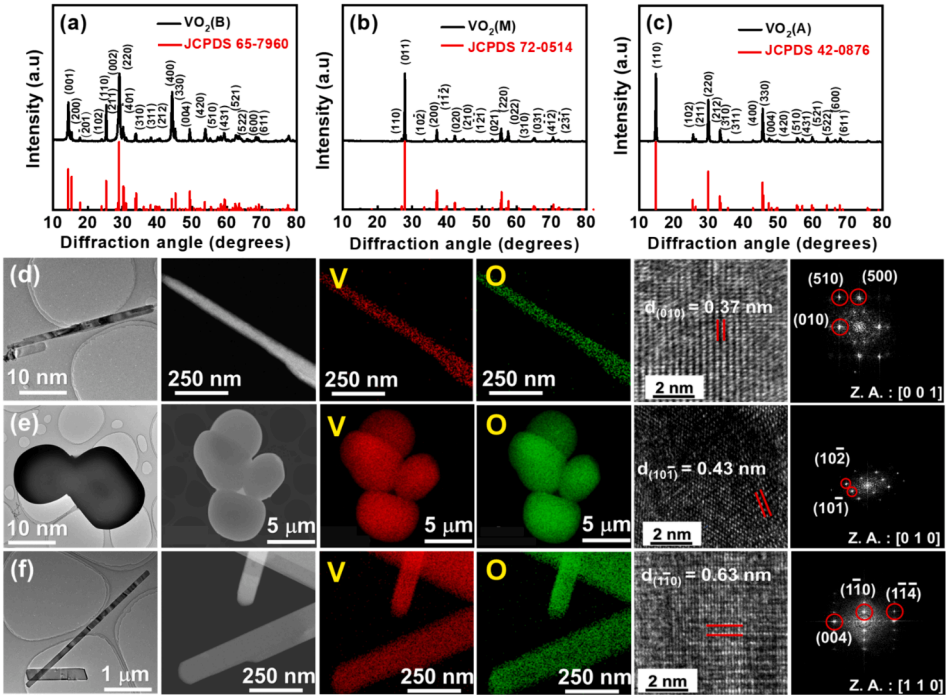

Fig. 1. (a–c) XRD patterns of various VO_2 polymorphs synthesized. High-resolution TEM analysis data for (d) VO_2 (B), (e) VO_2 (M), and (f) VO_2 (A) samples.

approximately 60 nm, which is larger than that for VO_2 (B). With well-distributed constituent elements, the crystallinity was confirmed to be tetragonal. **Fig. S1** shows SEM micrographs of the three VO_2 polymorphs. The microstructures are consistent with the TEM observations.

The initial three charge–discharge profiles of various VO_2 electrodes with the 1 m $ZnSO_4$ electrolyte are shown in Fig. 2 **a** — **c**. It can be seen that the charge–discharge curves of the VO_2 (B) and VO_2 (M) cathodes have similar shapes. These cathodes have reversible capacities of 340 and 305 mAh g^{-1}, respectively, at 0.1 A g^{-1}. However, the VO_2 (A) electrode exhibited rather different electrochemical behavior, with a major discharge plateau below 0.5 V. Besides the lower redox potential compared to those of VO_2 (B) and VO_2 (M), the VO_2 (A) electrode showed a relatively low capacity of 260 mAh g^{-1} at 0.1 A g^{-1}. The CE values for all electrodes are higher than 99 %. The VO_2 crystal structures significantly affect the number of charge storage sites, leading to distinct reversible capacities. Fig. 2 **d** — **f** shows the charge–discharge curves of the VO_2 electrodes measured under various current densities. VO_2 (B) outperformed the other two polymorphs, especially when operated at a high rate. The VO_2 (B) cathode retained ~70 % of its reversible capacity at 1.0 A g^{-1} (vs. the value obtained at 0.1 A g^{-1}), whereas the VO_2 (M) and VO_2 (A) cathodes retained only ~58 % and ~43 % of their capacities, respectively. It has been reported that VO_2 (B) has relatively high electronic conductivity [46] and wide one-dimensional tunnels along the *b* axis, which facilitate Zn^{2+} transport, leading to superior performance [21,22]. VO_2 (M) has a distorted crystal lattice, leading to crowded and narrow ion pathways, resulting in relatively poor rate performance compared to that of VO_2 (M) [47]. The VO_2 (A) phase belongs to the tetrahedral P42/ncm space group, where vanadium ions sit in a compressed octahedral environment. In this structure, the V^{4+}–V^{4+} chains connect to form a zigzag structure, which could hinder ion transport [48]. Moreover, VO_2 (A) has an insulating nature [49]. As a consequence, it showed inferior specific capacity and rate capability.

Table 1 shows the physicochemical properties of the $ZnSO_4$-based electrolytes used in this study. Tripling the $ZnSO_4$ concentration increased the ionic conductivity from 3.2 to 6.6 mS cm^{-1} because of the increased number of charge carriers. A concentration of 3 m is close to the solubility limit of $ZnSO_4$ in water; a further increase in $ZnSO_4$ content would lead to precipitation. Utilizing the LiTFSI additive effectively boosted ionic conductivity; the 1 m $ZnSO_4$/5 m LiTFSI dual-salt electrolyte had the highest conductivity (23.8 mS cm^{-1}). This is due to the fact that the bulky $TFSI^-$ anion can decrease the water number in the solvation shell of Li^+/Zn^{2+}. Such a reduced solvation effect can promote ionic transport [32,34,50]. However, the conductivity decreased to 17.5 mS cm^{-1} with 7 m LiTFSI additive; this is associated with high electrolyte viscosity due to the high salt concentration, which reduces ion mobility. It is difficult to add LiTFSI to the 3 m $ZnSO_4$ electrolyte because the excess LiTFSI is not soluble. Table 1 also shows that the electrolyte pH value decreases with increasing $ZnSO_4$ and LiTFSI concentrations, from pH=4.7 for 1 m $ZnSO_4$, pH=4.0 for 3 m $ZnSO_4$, to pH=3.0 for 1 m $ZnSO_4$/7 m LiTFSI electrolyte.

Table 1
The pH, ionic conductivity, and viscosity values of various electrolytes.

Electrolytes	pH	Conductivity (mS cm^{-1})	Viscosity (cP)
1 m $ZnSO_4$	4.7	3.2	5.7
3 m $ZnSO_4$	4.0	6.6	7.8
1 m $ZnSO_4$/3 m LiTFSI	3.4	15.6	8.9
1 m $ZnSO_4$/5 m LiTFSI	3.2	23.8	10.7
1 m $ZnSO_4$/7 m LiTFSI	3.0	17.5	12.3

LSV analysis was conducted to determine the electrochemical stability window of the formulated electrolytes. As shown in **Fig. S2**, the 1 m $ZnSO_4$ electrolyte starts to decompose at ~2.20 V. The oxygen evolution voltage increases to ~2.26 V when the $ZnSO_4$ concentration is increased to 3 m. After the incorporation of 5 m LiTFSI, no clear irreversible oxidation appears until ~2.30 V. The better electrolyte stability is attributed to the reduced water activity that originates from the high salt concentration [42,43,51,52]. It is noted that the decomposition voltage of the electrolytes is much higher than 1.5 V, which is the upper limit of the charge–discharge voltage window used in this study. Thus, there is little concern about electrolyte breakdown during cell operation.

Fig. 3**a and b** compares the charge–discharge curves of the VO_2 (B) electrode in 1 m $ZnSO_4$ and 3 m $ZnSO_4$ electrolytes, respectively. At a low rate (i.e., 0.1 A g^{-1}), the measured specific capacities in the two electrolytes are similar. At a higher current rate, the cell with 3 m $ZnSO_4$ electrolyte shows better performance, which is associated with the higher ionic conductivity of the electrolyte. As shown in Fig. 3**c–e**, the incorporation of LiTFSI up to a concentration of 5 m gradually increases the electrode capacity. For the 1 m $ZnSO_4$/5 m LiTFSI electrolyte, the reversible capacities are as high as 365 and 310 mAh g^{-1} at 0.1 and 1.0 A g^{-1}, respectively. A further increase in the LiTFSI concentration to 7 m caused electrode performance deterioration (i.e., 350 mAh g^{-1}@0.1 A g^{-1} and 290 mAh g^{-1}@1 A g^{-1}), which can be ascribed to the high viscosity and reduced ionic conductivity of the electrolyte. The CV data in **Fig. S3** show that the redox activity of the VO_2 (B) electrode in the 1 m $ZnSO_4$ electrolyte is much higher than that in the 5 m LiTFSI electrolyte.

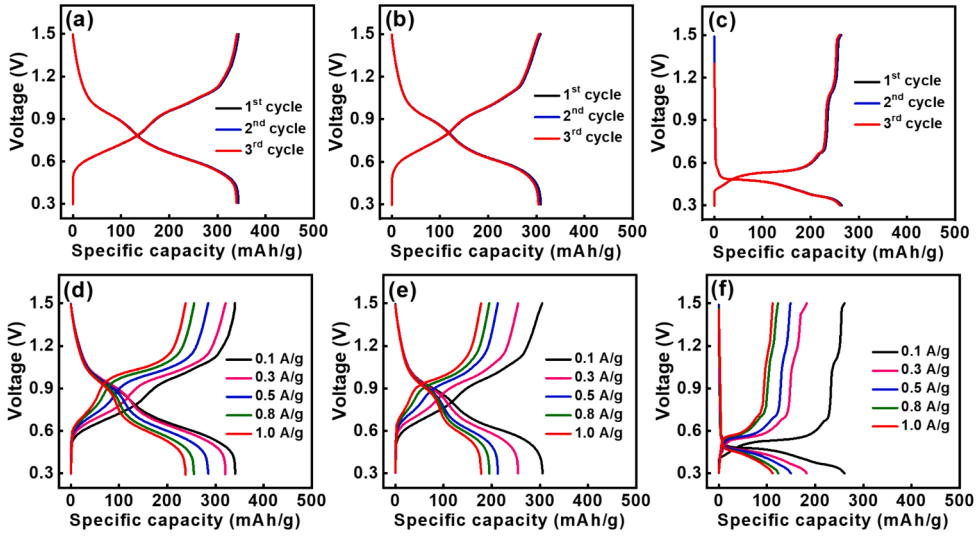

Fig. 2. (a–c) Initial three charge–discharge curves measured at 0.1 A/g and (d–f) charge–discharge curves measured at various rates for (a,d) VO_2 (B), (b,e) VO_2 (M), and (c,f) VO_2 (A) electrodes in 1 m $ZnSO_4$ electrolyte.

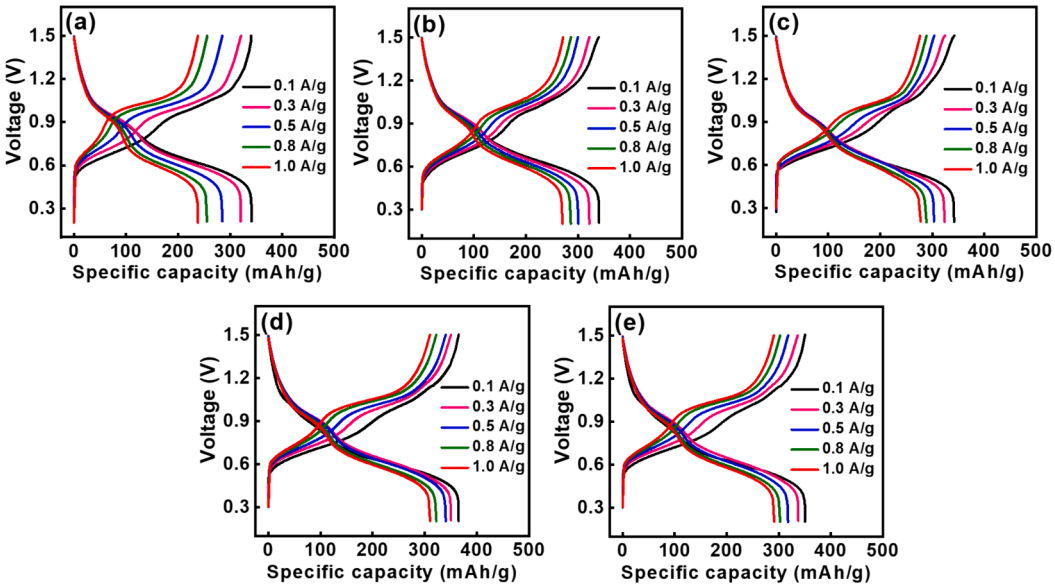

Fig. 3. Charge-discharge curves of VO_2 (B) electrodes measured in (a) 1 m $ZnSO_4$, (b) 3 m $ZnSO_4$, (c) 1 m $ZnSO_4$/3 m LiTFSI, (d) 1 m $ZnSO_4$/5 m LiTFSI, and (e) 1 m $ZnSO_4$/7 m LiTFSI electrolytes.

This indicates that the Zn^{2+} ion, rather than the Li^+ ion, is the dominant charge carrier in the charge storage reactions. In addition to increased conductivity, the improved capacity due to LiTFSI addition could also be related to increased proton activity in the electrolyte (see the pH values in Table 1). **Fig. S4** shows the charge–discharge curves of the VO_2 (B) electrode measured in the 1 m $ZnSO_4$/5 m $LiClO_4$ electrolyte. Interestingly, the electrode performance is much worse than that for the 1 m $ZnSO_4$/5 m LiTFSI electrolyte (see Fig. 3 **(d)**), indicating that the type of Li salt indeed matters. The counter anions of Li^+ can affect the salt dissociation degree in the electrolyte and thus alter solution coordination structures [42,43,51]. Therefore, the observed electrode charge–discharge properties are varied. It is noted that some experimental design methods, such as the response surface method [53], can be a powerful tool to further optimize the electrolyte recipe.

Fig. 4**a** compares the rate capability of the VO_2 (B) electrode in the 1 m $ZnSO_4$, 3 m $ZnSO_4$, and 1 m $ZnSO_4$/5 m LiTFSI electrolytes. The capacity retention of the electrode in these electrolytes at 1.0 A g^{-1} is 70 %, 79 %, and 85 %, respectively, compared to the values measured at 0.1 A g^{-1}. The causes of the rate capability difference were further examined using EIS. Fig. 4**b and c** shows the spectra acquired at 1.3 and 0.2 V, respectively. The EIS Nyquist spectra consist of a semicircle at high frequency and a sloping line at low frequency, which can be characterized by the equivalent circuit shown in the figure inset, where R_s, R_{ct}, *CPE*, and *W* represent the electrolyte resistance, charge transfer resistance at the electrode/electrolyte interface, interfacial constant-phase element, and Warburg impedance associated with charge carrier diffusion within the electrode, respectively [54]. The data fitting results are shown in Table 2. It is found that the R_{ct} values are significantly higher than the R_s values, indicating that the interfacial charge transfer properties, rather than the electrolyte conductivity, dominate the cell impedance. Of note, at 1.3 V, the R_{ct} values of the three cells are close to each other and much lower than those measured at 0.2 V. The higher impedance found at a lower voltage can be attributed to the formation of the $(Zn(OH)_2)_3(ZnSO_4)\cdot xH_2O$ byproduct during discharge, which covers the electrode surface and thus hinders charge transfer [55,56]. The R_{ct} values of the VO_2 (B) electrode in the 1 m $ZnSO_4$, 3 m $ZnSO_4$, and 1 m $ZnSO_4$/5 m LiTFSI electrolytes at 0.2 V are 589.1, 520.3, and 405.9 Ω, respectively. The relatively low R_s and R_{ct} values found for the last cell reflect that the charge carriers (Zn^{2+}, Li^+, and protons) can be easily transported in the electrolyte and across the electrode/electrolyte interface, leading to the superior rate capability.

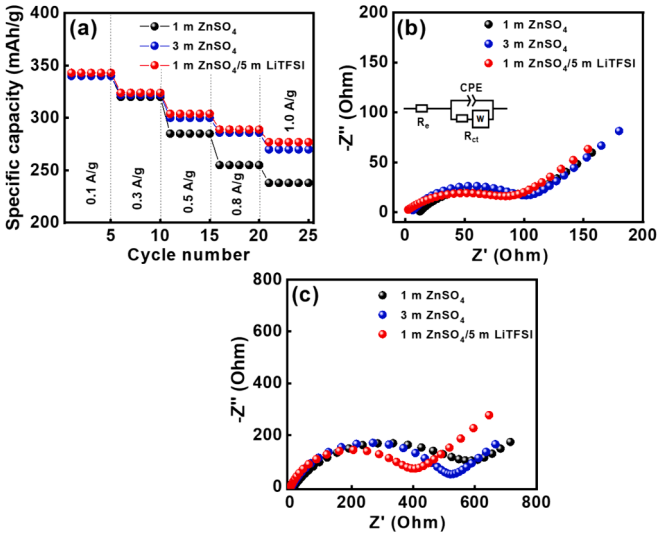

Fig. 4. (a) Comparative rate performance of VO_2 (B) electrodes in various electrolytes. EIS spectra of VO_2 (B) cells with various electrolytes measured at (b) 1.3 V and (c) 0.2 V.

GITT was used to determine the ion diffusion coefficients (*D*) of the VO_2 (B) electrode in various electrolytes. As shown in **Fig. S5**, in line with the EIS data, the ion transport is relatively sluggish at a low voltage, suggesting the formation of resistive species at the electrode. The average *D* values for the 1 m $ZnSO_4$, 3 m $ZnSO_4$, and 1 m $ZnSO_4$/5 m LiTFSI cells are 1.45×10^{-9}, 1.59×10^{-9}, and 1.81×10^{-9} cm^2 s^{-1}, respectively. The data are consistent with the R_{ct} results obtained from EIS measurements, explaining the high-rate performance variation of

Table 2
R_s and R_{ct} values of VO_2 (B) cells with various electrolytes measured using EIS.

Electrolytes	R_s @1.3 V	R_s @ 0.2 V	R_{ct} @1.3 V	R_{ct} @ 0.2 V
1 m $ZnSO_4$	12.4	12.5	99.1	589.1
3 m $ZnSO_4$	6.6	6.4	95.1	520.3
1 m $ZnSO_4$/5 m LiTFSI	2.0	1.9	89.1	405.9

the VO_2 (B) electrode in various electrolytes.

To understand the byproduct phase formed and the ion insertion degree of the VO_2 (B) electrode, XRD analyses were conducted; the data are shown in Fig. 5. VO_2 (B) cathodes were cycled five times and terminated at a discharged state (i.e., at 0.2 V) in the 1 m $ZnSO_4$, 3 m $ZnSO_4$, and 1 m $ZnSO_4$/5 m LiTFSI electrolytes. The electrodes were then subjected to XRD examination. For the 1 m $ZnSO_4$ electrolyte, new diffraction peaks that match $(Zn(OH)_2)_3(ZnSO_4)\cdot 4H_2O$ and $(Zn(OH)_2)_3(ZnSO_4)\cdot 5H_2O$ phases can be clearly observed. In this electrolyte, the Zn^{2+} ions easily form complexes with water molecules, such as $[Zn(H_2O)_6]^{2+}$ [38]. These complexes would be spontaneously transformed via:

$$\left[Zn(H_2O)_6\right]^{2+} + SO_4^{2-} \rightarrow \left[Zn(H_2O)_5(OH)\right]^{+} + HSO_4 \quad (1)$$

$$5\left[Zn(H_2O)_5(OH)\right]^{+} + 5HSO_4^{-} \rightarrow$$

$$\left(Zn(OH)_2\right)_3(ZnSO_4)\cdot 5H_2O\downarrow + 4HSO_4^{-} + 2H_3O^{+} + Zn^{2+} + 17H_2O \quad (2)$$

The insoluble $(Zn(OH)_2)_3(ZnSO_4)\cdot xH_2O$ product was precipitated and covered the electrode surface. As shown in Fig. 5, increasing the $ZnSO_4$ concentration to 3 m in the electrolyte reduces the $(Zn(OH)_2)_3(ZnSO_4)\cdot xH_2O$ peak intensity. This occurs because the water activity (and thus the $[Zn(H_2O)_6]^{2+}$ content) was decreased. This surface byproduct layer is most suppressed for the 1 m $ZnSO_4$/5 m LiTFSI electrolyte. This is associated with the fact that water molecules are most coordinated with the high-concentration Li^+ ions. In addition, the bulky $TFSI^-$ anions can decrease the interaction between Zn^{2+} ions and water molecules. As a result, a minimal amount of water molecules could surround Zn^{2+} ions to form $[Zn(H_2O)_6]^{2+}$. Also shown in Fig. 5 is a diffraction peak shift of the VO_2 (B) phase after discharging. This is associated with the VO_2 (B) lattice expansion due to the intercalation of the charge carriers. Of note, the peak shift amount depends on the electrolyte composition. The lattice parameters were determined based on the Rietveld refinement, as shown in Table S2. The largest lattice size of the VO_2 (B) discharged in the 1 m $ZnSO_4$/5 m LiTFSI electrolyte reflects the highest number of ions/protons inserted into the structure. This explains the superior measured capacity compared to those found for the 1 m $ZnSO_4$ and 3 m $ZnSO_4$ electrolytes. The $(Zn(OH)_2)_3(ZnSO_4)\cdot xH_2O$ side reaction product seems to hinder the intercalation reactions, leading to a decrease in the reversible capacity. The SEM images in Fig. S6 clearly show that the huge $(Zn(OH)_2)_3(ZnSO_4)\cdot xH_2O$ chunks that formed in the 1 m $ZnSO_4$ electrolyte, which could block ion/proton intercalation into the electrode, are greatly diminished when 5 m LiTFSI is added into the electrolyte.

WAXS was used to evaluate the solution structures of various electrolytes. Fig. 6**a** shows the data for the aqueous electrolytes with various concentrations of $ZnSO_4$. The broad peaks centered at ~2.02 and ~2.90 $Å^{-1}$ are associated with the oxygen–oxygen and oxygen–hydrogen correlations of the hydrogen-bonded network of H_2O molecules (i.e., bulk water). In the dilute electrolyte, even though some dipolar H_2O molecules coordinate with Zn^{2+} ions, forming hydrated $(Zn(H_2O)_6)^{2+}$ complex ions, because there are plenty of H_2O molecules, water peaks do not significantly change. With an increase in the $ZnSO_4$ concentration to 3 m, the water signal diminishes, and some extra peaks appear in the q range of 0.8–1.5 $Å^{-1}$ (marked by gray labels), indicating the formation of periodic structures in the electrolyte. The high population of Zn^{2+} and SO_4^{2-} ions suppresses the oxygen–oxygen correlation, decreasing the bulk water peak intensity. Instead, solvent-separated ion pairs (SSIP; $Zn^{2+}\cdots H_2O\cdots SO_4^{2-}$) and contact ion pairs (CIP; $Zn^{2+}\cdots SO_4^{2-}$) form. These periodic structures (i.e., charge-ordering structures) lead to the two extra peaks in the low-q region. However, due to the limited solubility of $ZnSO_4$ salt, the charge-ordering structures are not well developed. Because most H_2O molecules do not coordinate with ionic species, the bulk water peak is still pronounced. Fig. 6**b** shows the WAXS data for electrolytes with various concentrations of LiTFSI (without $ZnSO_4$). The high electron delocalization of $TFSI^-$ anions results in their low Coulombic interaction with Li^+ cations, leading to a high degree of salt dissociation and high solubility. With increasing LiTFSI concentration, because the water content becomes less (i.e., insufficient free H_2O molecules to keep the hydrogen-bonded water network), the bulk water peaks gradually diminish. Note that because of the weak scattering of X-rays by Li^+ ions, this interaction contributes little intensity to the WAXS pattern. The first charge-ordering peak (COP I) that emerges in the q range of 0.3 – 0.7 $Å^{-1}$ is associated with the solvated-TFSI structure

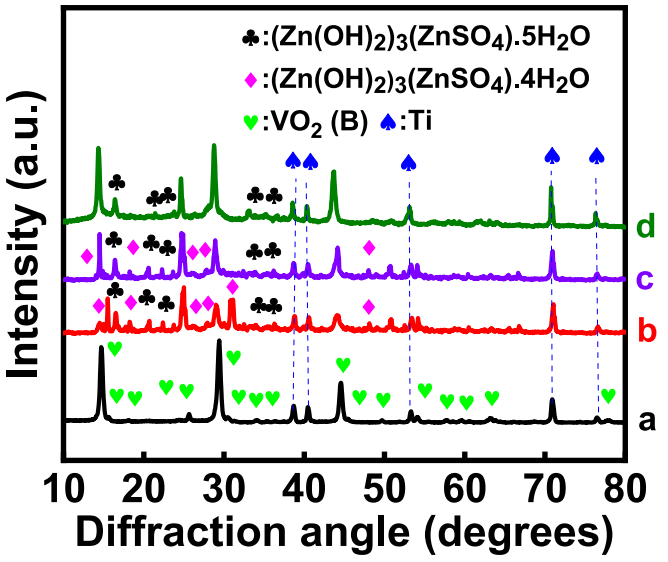

Fig. 5. XRD patterns of VO_2 (B) electrodes before (curve *a*) and after being cycled five times and discharged to 0.2 V in 1 m $ZnSO_4$ (curve *b*), 3 m $ZnSO_4$ (curve *c*), and 1 m $ZnSO_4$/5 m LiTFSI (curve *d*) electrolytes.

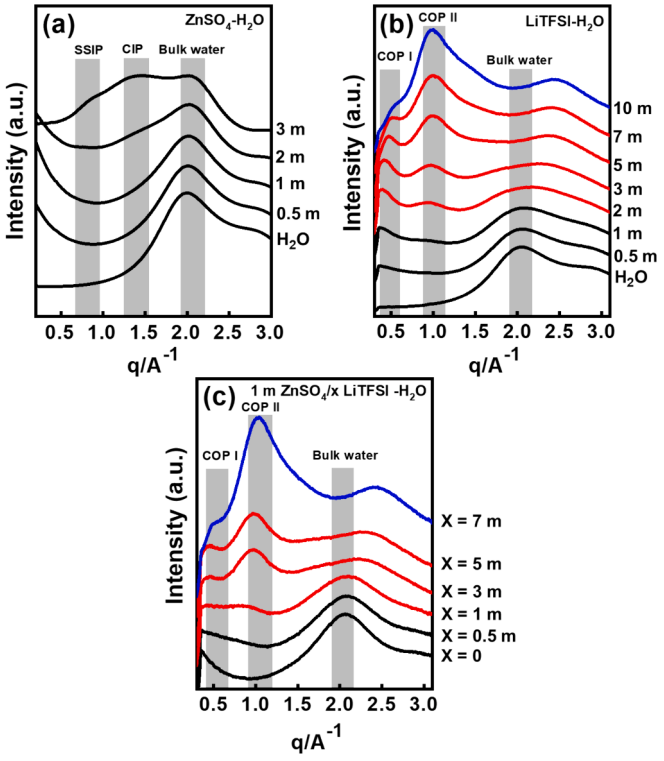

Fig. 6. WAXS patterns of electrolytes with (a) various concentrations of $ZnSO_4$, (b) various concentrations of LiTFSI, and (c) 1 m $ZnSO_4$ and various concentrations of LiTFSI.

(TFSI···H_2O···TFSI). In this case, an H_2O molecule bridges two adjacent $TFSI^-$ anions. As shown, this peak shifts from 0.39 $Å^{-1}$ (for 2 m LiTFSI) to 0.56 $Å^{-1}$ (for 10 m LiTFSI), indicating a shortening of the correlation distance between adjacent $TFSI^-$ ions due to the reduced content of water. The second charge-ordering peak (COP II) appears at ~0.99 $Å^{-1}$; it is related to the TFSI···TFSI correlation (i.e., direct contact between $TFSI^-$ ions without an H_2O bridge). With increasing LiTFSI concentration, this peak becomes stronger and sharper at the expense of the (TFSI···H_2O···TFSI) peak intensity. This reflects the formation of large ion aggregates when the water molecules become scarce. Moreover, at a high concentration of LiTFSI, a new peak emerges at ~2.5 $Å^{-1}$, which is associated with the intra-molecule structural feature of LiTFSI [57].

Fig. 6**c** shows the WAXS patterns for the 1 m $ZnSO_4$ electrolytes with various concentrations of LiTFSI. With the addition of LiTFSI, the intensity of the bulk water peak gradually decreases. LiTFSI, rather than $ZnSO_4$, seems to dominate the solution coordination structures due to its higher solubility and dissociation degree. With 3 m LiTFSI, COP I and COP II clearly appear. For 5 m LiTFSI, COP I and COP II are clearly stronger than the bulk water peak, explaining the lower $(Zn(OH)_2)_3(ZnSO_4)\cdot xH_2O$ formation found in Fig. 5 and **Fig. S6**. When the LiTFSI concentration reaches 7 m, COP II greatly intensifies, indicating the evolution of large ion aggregates, which may be the root cause of the reduced electrolyte conductivity (see Table 1). It is also noted that this COP II is at 1.01 $Å^{-1}$, which is greater than the value (0.99 $Å^{-1}$) for the COP II of the plain 7 m LiTFSI electrolyte (see **Fig. S7** for comparison). Moreover, the former COP II shows higher scattering intensity. This indicates that the Zn^{2+} ions promote the formation of ion pairs and aggregates. Because Zn^{2+} has a higher charge density than that of Li^+, the TFSI···TFSI distance can be shortened (since there is a stronger electrostatic force between cations and anions).

Operando TXM was used to examine the VO_2 (B) morphology variation during charge and discharge. Fig. 7**a and b** shows the obtained images taken in 1 m $ZnSO_4$ and 1 m $ZnSO_4$/5 m LiTFSI electrolytes, respectively, after two conditioning cycles. With the 1 m $ZnSO_4$ electrolyte, the VO_2 (B) rods were difficult to observe because of the accumulation of $(Zn(OH)_2)_3(ZnSO_4)\cdot xH_2O$ byproduct, which covered the entire electrode. In contrast, the morphology of VO_2 (B) can be clearly seen in the 1 m $ZnSO_4$/5 m LiTFSI electrolyte. This finding is consistent with the XRD and SEM results (see Fig. 5 and **Fig. S6**). As shown in Fig. 7**b**, upon charging, due to the ion/proton deintercalation, the VO_2 (B) rods show volume contraction. This contraction is reversible, as volume expansion occurs during discharging. However, as shown, the dimensional difference between the fully discharged and charged states is insignificant, namely ~10 % of the length of the VO_2 (B) rods. High dimensional stability of the active material during charging and discharging is essential for the long cycle life of the electrode.

At the anode side, LiTFSI addition also affects the redox behavior of the Zn electrode. Fig. 8**a** compares the Zn plating and stripping profiles recorded in Zn//Cu cells with 1 m $ZnSO_4$ and 1 m $ZnSO_4$/5 m LiTFSI electrolytes, respectively, at 0.5 mA cm^{-2}. As shown, the latter cell exhibits higher polarization during Zn deposition and dissolution. This can be attributed to the relatively high electrolyte viscosity of the 1 m $ZnSO_4$/5 m LiTFSI electrolyte and the hindrance effects of Li^+ and/or $TFSI^-$ near the electrode surface. As shown in Fig. 8**b**, the average CE for the 1 m $ZnSO_4$ and 1 m $ZnSO_4$/5 m LiTFSI cells was found to be 97.5 % and 99.0 %, respectively. With LiTFSI addition, the free water content in the electrolyte is reduced, and most of the water molecules are coordinated with Li^+ and $TFSI^-$ ions (see WAXS data), leading to a reduction in hydrogen evolution side reactions [58]. Fig. 8**b** also shows the cycling stability of the two Zn//Cu cells. The 1 m $ZnSO_4$ cell died at the 100th cycle, and the 1 m $ZnSO_4$/5 m LiTFSI cell survived until the 400th cycle before short-circuiting. Fig. 8**c and d** shows SEM images of the Zn deposited in 1 m $ZnSO_4$ and 1 m $ZnSO_4$/5 m LiTFSI, respectively, after 30 plating/stripping cycles. The latter morphology is flatter and more compact, which is related to less hydrogen gas evolution during cycling. Moreover, the abundant Li^+ ions accumulate in the vicinity of the protruding area of the electrode (due to a nonuniform electrical field), preventing further Zn dendrite growth [55]. Since the reduction potential of Li^+ ions is much lower than that of Zn^{2+} ions (−3.04 V vs. −0.76 V, respectively), Li^+ ions are not electroplated and thus serve as an electrostatic shielding agent that repels incoming Zn^{2+} ions from the protrusion, forcing further deposition of Zn to adjacent regions of the anode until a smooth electrode surface is formed [43,59]. Fig. 8**e and f** shows SEM micrographs of the Cu electrodes after Zn stripping in 1 m $ZnSO_4$ and 1 m $ZnSO_4$/5 m LiTFSI, respectively, after 30 cycles. There are some residual dead Zn compounds on the electrode when the former electrolyte is used. This is associated with the accumulation of zinc hydroxide sulfate byproducts and the broken mossy Zn that forms due to

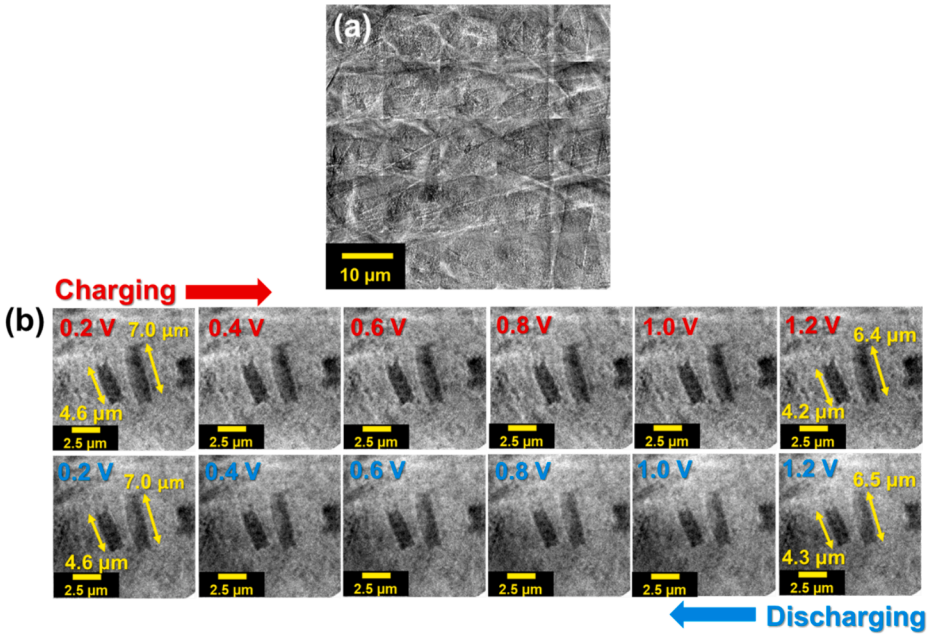

Fig. 7. (a) TXM images of VO_2 (B) observed in 1 m $ZnSO_4$ electrolyte. (b) TXM images of VO_2 (B) observed during charging and discharging in 1 m $ZnSO_4$/5 m LiTFSI electrolyte.

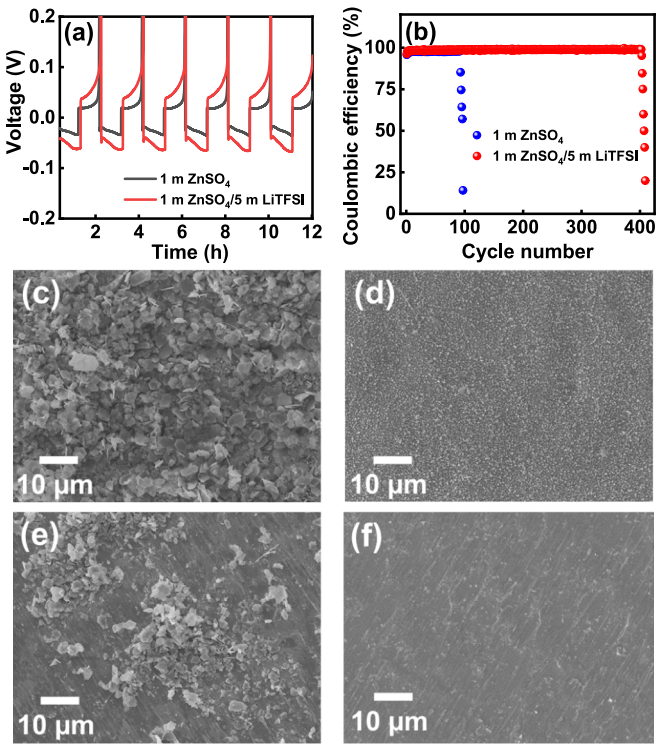

Fig. 8. (a) Zn plating/stripping curves and (b) the corresponding CE vs. cycle number profiles measured in 1 m $ZnSO_4$ and 1 m $ZnSO_4$/5 m LiTFSI electrolytes at 0.5 mA cm^{-2}. SEM images of electrodes after Zn plating in (c) 1 m $ZnSO_4$ and (d) 1 m $ZnSO_4$/5 m LiTFSI after 30 cycles. SEM images of electrodes after Zn stripping in (c) 1 m $ZnSO_4$ and (d) 1 m $ZnSO_4$/5 m LiTFSI after 30 cycles.

nonuniform Zn deposition and hydrogen bubble erosion [35]. The dead Zn compounds are electrically disconnected from the current collector and thus cannot be electro-stripped. In contrast, with 5 m LiTFSI addition into the electrolyte, the amount of dead Zn was significantly suppressed, which explains the superior anode cycling stability found in Fig. 8**b**.

Fig. 9 shows the cycling stability of Zn//VO_2 (B) cells with the 1 m $ZnSO_4$, 3 m $ZnSO_4$, and 1 m $ZnSO_4$/5 m LiTFSI electrolytes measured at 1.0 A g^{-1}. After 1000 charge–discharge cycles, the capacity retention ratios are 49 %, 63 %, and 90 %, respectively. Although increasing the $ZnSO_4$ concentration increases cyclability, the solubility of ~3 m limits the performance improvement. Adding 5 m LiTFSI to the electrolyte more effectively promotes cycle life. This is associated with the reduced $(Zn(OH)_2)_3(ZnSO_4)\cdot xH_2O$ passivation layer at the cathode side and the suppressed hydrogen evolution and Zn dendrite formation at the anode side.

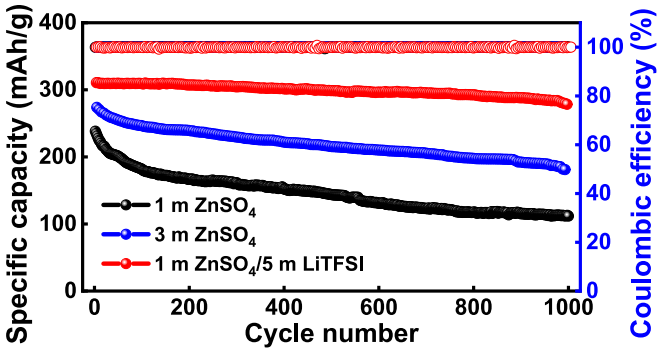

Fig. 9. Cycling stability data of Zn//VO_2 (B) cells with various electrolytes measured at 1.0 A/g.

We also studied the effects of electrolyte composition on the electrochemical properties of the VO_2 (M) cathode. Although the charge–discharge performance of VO_2 (M) is generally lower than that of VO_2 (B), as shown in Fig. S8, the reversible capacities and rate capability obtained with the 1 m $ZnSO_4$/5 m LiTFSI electrolyte are better than those obtained with the 1 m $ZnSO_4$ and 3 m $ZnSO_4$ electrolytes. This trend is consistent with that observed for VO_2 (B). The addition of 5 m LiTFSI effectively reduces the $(Zn(OH)_2)_3(ZnSO_4)\cdot xH_2O$ byproduct on the VO_2 (M) cathode (Figs. S9 and S10) and thus decreases the electrode charge-transfer impedance (Fig. S11). Moreover, the cycling stability of the Zn//VO_2 (M) cells was clearly improved (to ~90 % retention after 1000 cycles) due to 5 m LiTFSI addition (Fig. S12). The proposed 1 m $ZnSO_4$/5 m LiTFSI electrolyte is cost-effective and enhances the reversible capacities, rate capability, and cycling stability of ZIBs with VO_2-type cathodes.

4. Conclusions

This study synthesized three VO_2 polymorphs and investigated their microstructures and electrochemical properties for application in ZIBs. It was found that VO_2 (B) outperforms VO_2 (M) and VO_2 (A) in terms of the specific capacity and rate capability (340 and 238 mAh g^{-1} at 0.1 and 1.0 A g^{-1}, respectively) due to its relatively large number of charge storage sites, high electronic conductivity, and wide structural tunnels that can facilitate Zn^{2+} transport. Increasing the $ZnSO_4$ concentration in the electrolyte from 1 m to 3 m marginally improves the electrode charge–discharge performance, which is associated with increased electrolyte conductivity. However, because of the solubility limit, it is difficult to increase the $ZnSO_4$ concentration further. According to the WAXS data, the charge-ordering structures of the 3 m $ZnSO_4$ electrolyte are not well developed, and the bulk water feature is still pronounced. The incorporation of LiTFSI greatly alters the solution structures. When the LiTFSI concentration is increased to 5 m, the intensity of the bulk water peak gradually diminishes, and COP I (related to TFSI···H_2O···TFSI) and COP II (related to TFSI···TFSI) clearly evolve. Because of the reduced water activity, the anodic limit (that related to oxygen evolution from the decomposition of water) of the electrolyte is extended, and the Zn $(OH)_2)_3(ZnSO_4)\cdot xH_2O$ byproduct formation tendency is suppressed. The thinner byproduct layer, which reduces the blocking of ion/proton intercalation reactions, is responsible for the excellent charge–discharge properties of the VO_2 electrode obtained with the 1 m $ZnSO_4$/5 m LiTFSI dual-salt electrolyte. The unique solution structure of this electrolyte also alleviates the hydrogen evolution side reaction, leads to flat and compact Zn deposits, and reduces the amount of dead Zn on the electrode after cycling. However, if the LiTFSI content is excessive (i.e., 7 m), large ion aggregates form, leading to the deterioration of the electrolyte conductivity and VO_2 electrode performance. The VO_2 electrode has great dimensional reversibility and stability during cycling in the 1 m $ZnSO_4$/5 m LiTFSI electrolyte, as verified via operando TXM. The proposed electrode/electrolyte design strategies and the solution structure approach are expected to be important for the further development of ZIBs.

CRediT authorship contribution statement

Jing-Hong Huang: Methodology, Investigation, Formal analysis, Data curation. **Xu-Feng Luo:** Methodology, Investigation, Formal analysis. **Tzu-Yu Kuo:** Investigation, Formal analysis. **Yu-Hua Lai:** Investigation, Formal analysis. **Purna Chandra Rath:** Writing – original draft, Data curation. **Chun-Wei Huang:** Methodology, Formal analysis. **Ming-Hsien Lin:** Methodology, Investigation, Formal analysis. **An-Yuan Hou:** Investigation, Formal analysis, Data curation. **Ju Li:** Writing – review & editing, Validation. **Yu-Sheng Su:** Writing – original draft, Data curation. **Wen-Wei Wu:** Writing – review & editing, Methodology, Data curation. **Jeng-Kuei Chang:** Writing – review & editing, Visualization, Supervision, Project administration, Methodology, Funding

acquisition, Data curation, Conceptualization.

Declaration of competing interest

The authors declare that they have no known competing financial interests or personal relationships that could have appeared to influence the work reported in this paper.

Data availability

Data will be made available on request.

Acknowledgments

This work is supported by the "Future Semiconductor Technology Research Center" from The Featured Areas Research Center Program within the framework of the Higher Education Sprout Project by the Ministry of Education (MOE) in Taiwan. This work is also financially supported the National Science and Technology Council, Taiwan, under Grant Nos. NSTC 113-2634-F-A49-008, NSTC 112-2628-E-A49-026, and NSTC 112-2923-E-007-005.

Appendix A. Supplementary data

Supplementary data to this article can be found online at https://doi.org/10.1016/j.cej.2024.154609.

References

[1] M. Armand, J.M. Tarascon, Building better batteries, Nature 451 (2008) 652–657, https://doi.org/10.1038/451652a.
[2] D. Larcher, J.M. Tarascon, Towards greener and more sustainable batteries for electrical energy storage, Nat. Chem. 7 (2015) 19–29, https://doi.org/10.1038/nchem.2085.
[3] H.M.A. Amin, C. Molls, P.P. Bawol, H. Baltruschat, The impact of solvent properties on the performance of oxygen reduction and evolution in mixed tetraglyme-dimethyl sulfoxide electrolytes for Li-O_2 batteries: Mechanism and stability, Electrochim. Acta 245 (2017) 967–980, https://doi.org/10.1016/j.electacta.2017.06.012.
[4] D. Wittmaier, N. Wagner, K.A. Friedrich, M.A. Hatem, H.B. Amin, Modified carbon-free silver electrodes for the use as cathodes in lithium-air batteries with an aqueous alkaline electrolyte, J. Power Sources 265 (2014) 299–308, https://doi.org/10.1016/j.jpowsour.2014.04.142.
[5] B. Dunn, H. Kamath, J.M. Tarascon, Electrical energy storage for the grid: A battery of choices, Science 334 (2011) 928–935, https://doi.org/10.1126/science.1212741.
[6] J. Xu, X. Cai, S. Cai, Y. Shao, C. Hu, S. Lu, S. Ding, High-energy lithium-ion batteries: Recent progress and a promising future in applications, Energy Environ. Mater. 6 (2023) e12450.
[7] R. Schmuch, R. Wagner, G. Hörpel, T. Placke, M. Winter, Performance and cost of materials for lithium-based rechargeable automotive batteries, Nat. Energy 3 (2018) 267–278, https://doi.org/10.1038/s41560-018-0107-2.
[8] L. Lu, X. Han, J. Li, J. Hua, M. Ouyang, A review on the key issues for lithium-ion battery management in electric vehicles, J. Power Sources 226 (2013) 272–288, https://doi.org/10.1016/j.jpowsour.2012.10.060.
[9] J. Yue, S. Chen, J. Yang, S. Li, G. Tan, R. Zhao, C. Wu, Y. Bai, Multi-ion engineering strategies toward high performance aqueous zinc-based batteries, Adv. Mater. 36 (2023) 2304040, https://doi.org/10.1002/adma.202304040.
[10] M. Huang, X. Wang, X. Liu, L. Mai, Fast ionic storage in aqueous rechargeable batteries: From fundamentals to applications, Adv. Mater. 34 (2022) 2105611, https://doi.org/10.1002/adma.202105611.
[11] B. Yong, D. Ma, Y. Wang, H. Mi, C. He, P. Zhang, Understanding the design principles of advanced aqueous zinc-ion battery cathodes: From transport kinetics to structural engineering, and future perspectives, Adv. Energy Mater. 10 (2020) 2002354, https://doi.org/10.1002/aenm.202002354.
[12] X. Chen, W. Li, D. Reed, X. Li, X. Liu, On energy storage chemistry of aqueous Zn-ion batteries: From cathode to anode, Electrochem. Energy Rev. 6 (2023) 33, https://doi.org/10.1007/s41918-023-00194-6.
[13] S. Gull, H.Y. Chen, Recent advances in cathode materials for aqueous zinc-ion batteries: Mechanisms, materials, challenges, and opportunities, MRS Energy Sustain. 9 (2022) 248–280, https://doi.org/10.1557/s43581-022-00044-w.
[14] T.F. Yi, L. Qiu, J.P. Qu, H. Liu, J.H. Zhang, Y.R. Zhu, Towards high-performance cathodes: Design and energy storage mechanism of vanadium oxides-based materials for aqueous Zn-ion batteries, Coord. Chem. Rev. 446 (2021) 214124, https://doi.org/10.1016/j.ccr.2021.214124.
[15] L.E. Blanc, D. Kundu, L.F. Nazar, Scientific challenges for the implementation of Zn-ion batteries, Joule 4 (2020) 771–799, https://doi.org/10.1016/j.joule.2020.03.002.
[16] G. Zampardi, F.L. Mantia, Prussian blue analogues as aqueous Zn-ion batteries electrodes: Current challenges and future perspectives, Curr. Opin. Electrochem. 21 (2020) 84–92, https://doi.org/10.1016/j.coelec.2020.01.014.
[17] T. Zhao, H. Wu, X. Wen, J. Zhang, H. Tang, Y. Deng, S. Liao, X. Tian, Recent advances in MOFs/MOF derived nanomaterials toward high-efficiency aqueous zinc ion batteries, Coord. Chem. Rev. 468 (2022) 214642, https://doi.org/10.1016/j.ccr.2022.214642.
[18] G. Li, L. Sun, S. Zhang, C. Zhang, H. Jin, K. Davey, G. Liang, S. Liu, J. Mao, Z. Guo, Developing cathode materials for aqueous zinc ion batteries: Challenges and practical prospects, Adv. Funct. Mater. 34 (2024) 2301291, https://doi.org/10.1002/adfm.202301291.
[19] P. Hu, P. Hu, T.D. Vu, M. Li, S. Wang, Y. Ke, X. Zeng, L. Mai, Y. Long, Vanadium oxide: Phase diagrams, structures, synthesis, and applications, Chem. Rev. 123 (2023) 4353–4415, https://doi.org/10.1021/acs.chemrev.2c00546.
[20] Y. Liu, X. Wu, Review of vanadium-based electrode materials for rechargeable aqueous zinc ion batteries, J. Energy Chem. 56 (2021) 223–237, https://doi.org/10.1016/j.jechem.2020.08.016.
[21] Z. Khan, P. Singh, S.A. Ansari, S.R. Manippady, A. Jaiswal, M. Saxena, VO_2 nanostructures for batteries and supercapacitors: A review, Small 17 (2021) 2006651, https://doi.org/10.1002/smll.202006651.
[22] W. Zhang, W. Zhong, J. Wang, Q. An, L. Mai, Current challenges and advanced design strategy of vanadium dioxide cathode for low-cost aqueous zinc metal battery, Adv. Energy Sustain. Res. 4 (2023) 2300139, https://doi.org/10.1002/aesr.202300139.
[23] L. Kou, Y. Wang, J. Song, T. Ai, W. Li, P. Wattanapaphawong, K. Kajiyoshi, One-dimensional tunnel VO $_2$ (B) cathode materials for high-performance aqueous zinc ion batteries: A mini review of recent advances and future perspectives, Green Chem. 26 (2024) 1709–1724, https://doi.org/10.1039/D3GC03887D.
[24] S.S. Saeidi, B. Vaseghi, G. Rezaei, H. Khajehsharifi, D. Jenkins, Magnetic, optical and phase transformation properties of Fe and Co doped VO_2 (A) nanobelts, J. Solid State Chem. 306 (2022) 122729, https://doi.org/10.1016/j.jssc.2021.122729.
[25] Y. Zhang, VO_2 (B) conversion to VO_2 (A) and VO_2 (M) and their oxidation resistance and optical switching properties, Mater. Sci. Pol. 34 (2016) 169–176, https://doi.org/10.1515/msp-2016-0023.
[26] A. Srivastava, H. Rotella, S. Saha, B. Pal, G. Kalon, S. Mathew, M. Motapothula, M. Dykas, P. Yang, E. Okunishi, D.D. Sarma, T. Venkatesan, Selective growth of single phase VO_2 (A, B, and M) polymorph thin films, APL Materials 3 (2015) 026101, https://doi.org/10.1063/1.4906880.
[27] J. Ding, Z. Du, L. Gu, B. Li, L. Wang, S. Wang, Y. Gong, S. Yang, Ultrafast Zn^{2+} intercalation and deintercalation in vanadium dioxide, Adv. Mater. 30 (2018) 1800762, https://doi.org/10.1002/adma.201800762.
[28] L. Zhang, L. Miao, B. Zhang, J. Wang, J. Liu, Q. Tan, H. Wan, J. Jiang, A durable VO_2 (M)/Zn battery with ultrahigh rate capability enabled by pseudocapacitive proton insertion, J. Mater. Chem. A 8 (2020) 1731–1740, https://doi.org/10.1039/C9TA11031C.
[29] Y. Liu, P. Hu, H. Liu, X. Wu, C. Zhi, Tetragonal VO_2 hollow nanospheres as robust cathode material for aqueous zinc ion batteries, Mater. Today Energy 17 (2020) 100431, https://doi.org/10.1016/j.mtener.2020.100431.
[30] Z. Ye, Z. Cao, M.O.L. Chee, P. Dong, P.M. Ajayan, J. Shen, M. Ye, Advances in Zn-ion batteries via regulating liquid electrolyte, Energy Storage Mater. 32 (2020) 290–305, https://doi.org/10.1016/j.ensm.2020.07.011.
[31] Z. Khan, D. Kumar, X. Crispin, Does Water-in-salt electrolyte subdue issues of Zn batteries? Adv. Mater. 35 (2023) 2300369, https://doi.org/10.1002/adma.202300369.
[32] P. Samanta, S. Ghosh, A. Kundu, P. Samanta, N.C. Murmu, T. Kuila, Recent progress on the performance of Zn-ion battery using various electrolyte salt and solvent concentrations, ACS Appl. Electron. Mater. 5 (2023) 100–116, https://doi.org/10.1021/acsaelm.2c01355.
[33] Y. Du, Y. Li, B.B. Xu, T.X. Liu, X. Liu, F. Ma, X. Gu, C. Lai, Electrolyte salts and additives regulation enables high performance aqueous zinc ion batteries: A mini review, Small 18 (2022) 2104640, https://doi.org/10.1002/smll.202104640.
[34] C. Liu, X. Xie, B. Lu, J. Zhou, S. Liang, Electrolyte strategies toward better zinc-ion batteries, ACS Energy Lett. 6 (2021) 1015–1033, https://doi.org/10.1021/acsenergylett.0c02684.
[35] F. Yang, J.A. Yuwono, J. Hao, J. Long, L. Yuan, Y. Wang, S. Liu, Y. Fan, S. Zhao, K. Davey, Z. Guo, Understanding H_2 evolution electrochemistry to minimize solvated water impact on zinc-anode performance, Adv. Mater. 34 (2022) 2206754, https://doi.org/10.1002/adma.202206754.
[36] Z. Cai, J. Wang, Y. Sun, Anode corrosion in aqueous Zn metal batteries, eScience 3 (2023) 100093, https://doi.org/10.1016/j.esci.2023.100093.
[37] Y. Zhou, G. Li, S. Feng, H. Qin, Q. Wang, F. Shen, P. Liu, Y. Huang, H. He, Regulating Zn ion desolvation and deposition chemistry toward durable and fast rechargeable Zn metal batteries, Adv. Sci. 10 (2023) 2205874, https://doi.org/10.1002/advs.202205874.
[38] J. Yang, B. Yin, Y. Sun, H. Pan, W. Sun, B. Jia, S. Zhang, T. Ma, Zinc anode for mild aqueous zinc-ion batteries: Challenges, strategies, and perspectives, Nano Micro Lett. 14 (2022) 42, https://doi.org/10.1007/s40820-021-00782-5.
[39] B.W. Olbasa, F.W. Fenta, S.F. Chiu, M.C. Tsai, C.J. Huang, B.A. Jote, T.T. Beyene, Y.F. Liao, C.H. Wang, W.N. Su, H. Dai, B.J. Hwang, High-rate and long-cycle stability with a dendrite-free zinc anode in an aqueous Zn-ion battery using concentrated electrolytes, ACS Appl. Energy Mater. 3 (2020) 4499–4508, https://doi.org/10.1021/acsaem.0c00183.

[40] D. Batyrbekuly, B. Laïk, J.P. Ramos, Z. Bakenov, R.B. Hadjean, A porous puckered V_2O_5 polymorph as new high performance cathode material for aqueous rechargeable zinc batteries, J. Energy Chem. 61 (2021) 459–468, https://doi.org/10.1016/j.jechem.2021.01.042.
[41] K.A. Owusu, X. Pan, R. Yu, L. Qu, Z. Liu, Z. Wang, M. Tahir, W.A. Haider, L. Zhou, L. Mai, Introducing Na_2SO_4 in aqueous $ZnSO_4$ electrolyte realizes superior electrochemical performance in zinc-ion hybrid capacitor, Mater. Today Energy 18 (2020) 100529, https://doi.org/10.1016/j.mtener.2020.100529.
[42] L. Suo, O. Borodin, T. Gao, M. Olguin, J. Ho, X. Fan, C. Luo, C. Wang, K. Xu, "Water-in-salt" electrolyte enables high-voltage aqueous lithium-ion chemistries, Science 350 (2015) 938–943, https://doi.org/10.1126/science.aab1595.
[43] F. Wang, O. Borodin, T. Gao, X. Fan, W. Sun, F. Han, A. Faraone, J.A. Dura, K. Xu, C. Wang, Highly reversible zinc metal anode for aqueous batteries, Nat. Mater. 17 (2018) 543–549, https://doi.org/10.1038/s41563-018-0063-z.
[44] S.P. Rao, M. Miclau, A. Artemenko, C. Labrugere, A. Villesuzanne, M. Pollet, Rapid hydrothermal synthesis of VO_2 (B) and its conversion to thermochromic VO_2 (M1), Inorganic Chem. 52 (2013) 4780–4785, https://doi.org/10.1021/ic301201k.
[45] H.P. Klug, L.E. Alexander, X-Ray Diffraction Procedures: For polycrystalline and amorphous materials, John Wiley & Sons Inc, New York, USA, 1974.
[46] S. Lee, I.N. Ivanov, J.K. Keum, H.N. Lee, Epitaxial stabilization and phase instability of VO_2 polymorphs, Sci. Rep. 6 (2016) 19621, https://doi.org/10.1038/srep19621.
[47] L. Wu, H. Fu, S. Li, J. Zhu, J. Zhou, A.M. Rao, L. Cha, K. Guo, S. Wen, B. Lu, Phase-engineered cathode for super-stable potassium storage, Nat. Commun. 14 (2023) 644, https://doi.org/10.1038/s41467-023-36385-4.
[48] S.R. Popuri, A. Artemenko, C. Labrugere, M. Miclau, A. Villesuzanne, M. Pollet, VO_2 (A): Reinvestigation of crystal structure, phase transition and crystal growth mechanisms, J. Solid State Chem. 213 (2014) 79–86, https://doi.org/10.1016/j.jssc.2014.01.037.
[49] S.S. Majid, A. Ahad, F. Rahman, V. Sathe, D. Shukla, Unveiling the role of VO_2 (B) polymorph in the insulator–metal transition of VO_2 (M1) thin films, Phys. Status Solidi (b) 259 (2022) 2200108, https://doi.org/10.1002/pssb.202200108.
[50] E.N. Saw, K. Kanokkanchana, H.M.A. Amin, K. Tschulik, Unravelling anion solvation in water-alcohol mixtures by single entity electrochemistry, ChemElectroChem 9 (2022) e202101435.
[51] J. Shin, J. Lee, Y. Park, J.W. Choi, Aqueous zinc ion batteries: Focus on zinc metal anodes, Chem. Sci. 11 (2020) 2028–2044, https://doi.org/10.1039/D0SC00022A.
[52] M. Turgeman, V.W. Fisher, F. Malchik, A. Saha, G. Bergman, B. Gavriel, T.R. Penki, A. Nimkar, V. Baranauskaite, H. Aviv, M.D. Levi, M. Noked, D.T. Major, N. Shpigel, D. Aurbach, A cost-effective water-in-salt electrolyte enables highly stable operation of a 2.15-V aqueous lithium-ion battery, Cell Rep. Phys. Sci. 3 (2022) 100688, https://doi.org/10.1016/j.xcrp.2021.100688.
[53] S. Ahmadi, A., Khormali Optimization of the corrosion inhibition performance of 2-mercaptobenzothiazole for carbon steel in HCl media using response surface methodology, Fuel 357 (2024) 129783, https://doi.org/10.1016/j.fuel.2023.129783.
[54] B. Umesh, P.C. Rath, R.F.H. Hernandha, J.Y. Lin, S.B. Majumder, Q.F. Dong, J. K. Chang, Moderate-concentration fluorinated electrolyte for high-energy-density Si//$LiNi_{0.8}Co_{0.1}Mn_{0.1}O_2$ batteries, ACS Sustainable, Chem. Eng. 8 (2020) 16252–16261, https://doi.org/10.1021/acssuschemeng.0c05560.
[55] K. Zhao, G. Fan, J. Liu, F. Liu, J. Li, X. Zhou, Y. Ni, M. Yu, Y.M. Zhang, H. Su, Q. Liu, F. Cheng, Boosting the kinetics and stability of Zn anodes in aqueous electrolytes with supramolecular cyclodextrin additives, J. Am. Chem. Soc. 144 (2022) 11129–11137, https://doi.org/10.1021/jacs.2c00551.
[56] Y. Zhuang, Y. Xie, B. Fei, D. Cai, Y. Wang, Q. Chen, H. Zhan, Construction of molybdenum vanadium oxide/nitride hybrid nanoplate arrays for aqueous zinc-ion batteries and reliable insights into the reaction mechanism, J. Mater. Chem. A 9 (2021) 21313–21322, https://doi.org/10.1039/D1TA05982C.
[57] K. Shimizu, A.A. Freitas, R. Atkin, G.G. Warr, P.A. FitzGerald, H. Doi, S. Saito, K. Ueno, Y. Umebayashi, M. Watanabe, J.N.C. Lopes, Structural and aggregate analyses of (Li salt + glyme) mixtures: The complex nature of solvate ionic liquids, Phys. Chem. Chem. Phys. 17 (2015) 22321–22335, https://doi.org/10.1039/C5CP03414K.
[58] M. Xu, T. Zhu, J.Z.H. Zhang, Molecular dynamics simulation of zinc ion in water with an ab-initio based neural network potential, J. Phys. Chem. A 123 (2019) 6587–6595, https://doi.org/10.1021/acs.jpca.9b04087.
[59] X. Guo, Z. Zhang, J. Li, N. Luo, G.L. Chai, T.S. Miller, F. Lai, P. Shearing, D.J. L. Brett, D. Han, Z. Weng, G. He, I.P. Parkin, Alleviation of dendrite formation on zinc anodes via electrolyte additives, ACS Energy Lett. 6 (2021) 395–403, https://doi.org/10.1021/acsenergylett.0c02371.